Microwave ac Zeeman force for ultracold atoms

C. T. Fancher,[*] A. J. Pyle, A. P. Rotunno, and S. Aubin

Department of Physics, College of William and Mary, Williamsburg, Virginia 23187, USA

We measure the ac Zeeman force on an ultracold gas of ^{87}Rb due to a microwave magnetic field targeted to the 6.8 GHz hyperfine splitting of these atoms. An atom chip produces a microwave near field with a strong amplitude gradient, and we observe a force over three times the strength of gravity. Our measurements are consistent with a simple two-level theory for the ac Zeeman effect and demonstrate its resonant, bipolar, and spin-dependent nature. We observe that the dressed-atom eigenstates gradually mix over time and have mapped out this behavior as a function of magnetic field and detuning. We demonstrate the practical spin selectivity of the force by pushing or pulling a specific spin state while leaving other spin states unmoved.

I. INTRODUCTION

Atomic physics has developed a formidable toolbox of experimental techniques for precision control of the external and internal states of atoms. The quantum control of internal states has led to the development of Ramsey interferometry [1], atomic clocks [2–4], and spin-polarized gases [5,6], among other applications. The precision control of the external degrees of freedom using laser cooling, evaporative cooling, and optical and magnetic traps are the key techniques for producing ultracold quantum gases [7,8]. Notably, however, methods that couple internal and external control remain more challenging and less versatile: optical Raman pulses can selectively kick a given spin state, but cannot trap it. A dc magnetic field produces spin-dependent potentials for each spin state, but these are all proportional. Optical dipole potentials at a magic wavelength behave similarly or must be periodic [9–11].

The ac Zeeman (ACZ) effect can be used to produce fully spin-dependent potentials and is a versatile addition to the quantum control toolbox [12–14]. In principle, multiple spin states can be selectively targeted with qualitatively different and independent potentials simultaneously. ACZ forces are broadly applicable to atomic systems with nondegenerate spin states. The ACZ force is resonant and bipolar, such that any hyperfine state can be either a weak- or strong-field seeker [15]. In the case of alkali hyperfine ground states, the relevant transitions are in the microwave (μw) and so are essentially immune to spontaneous emission.

However, since first being proposed and implemented for atomic beam [12,13] and cold atom systems [15,16], ACZ potentials have seen only occasional use due to the limitations of propagating (far-field) μw fields. The length scale for intensity variations in the far field is given by the wavelength (cm scale or larger), which severely limits the gradients and ACZ forces that are feasible at practical μw powers. For example, the ACZ potential produced by a μw power buildup cavity in Ref. [16]

was sufficient for weak horizontal confinement of cold atoms, but could not hold these against gravity.

More recently, strong ACZ forces have become feasible with atom chip–based μw near fields, in which the length scale for field variations is set by the geometry of the μw currents. This technology change has enabled the use of ACZ potentials for spin-dependent interferometry [17], spin squeezing, and ion-based quantum gates [18,19]. However, despite these recent applications, the ACZ effect has not been studied experimentally on its own. We note that ACZ potentials are distinct from adiabatic rf potentials [20], though both effects can be present simultaneously. ACZ potentials use a uniform dc magnetic field and produce a force with an ac field gradient. Adiabatic rf potentials produce a force with a dc magnetic gradient and use an ac field to couple dc high field–seeking and dc low field–seeking spin states.

We describe our experimental system (Sec. II) and present the first detailed measurements of the ACZ force in an ultracold gas of neutral ^{87}Rb atom and find reasonable agreement with two-level dressed-atom theory (Sec. III). We study the time evolution of a μw-dressed spin state as a function of magnetic field and detuning (Sec. IV). Finally, we use the ACZ force to push, pull, and remove a specific spin state within a spin mixture (Sec. V).

II. EXPERIMENTAL SYSTEM

In the $5S_{1/2}$ ground levels of ^{87}Rb [see Fig. 1(a)], the $|e\rangle = |F = 2, m_F = 2\rangle$ and $|g\rangle = |1,1\rangle$ hyperfine states form an effective two-level system with transition energy $\hbar\omega_0$. When driven by a μw magnetic field B_{ac} at frequency ω_{ac} and detuning $\delta = \omega_{ac} - \omega_0$, atoms in $|e\rangle$ can only transition to $|g\rangle$ directly. Atoms in $|g\rangle$ can transition to $|e\rangle$, $|2,1\rangle$, and $|2,0\rangle$, though off-resonant excitation of these last two is suppressed for large energy separations.

Following the original treatment of Agosta *et al.* [15], we use a dressed-atom basis $\{|g,N\rangle, |e,N-1\rangle\}$ to describe an N photon μw field and a two-level atom. Alternatively, an equivalent semiclassical treatment of the μw field uses the $\{|g\rangle, |e\rangle\}$ basis of bare atomic states in a rotating frame.
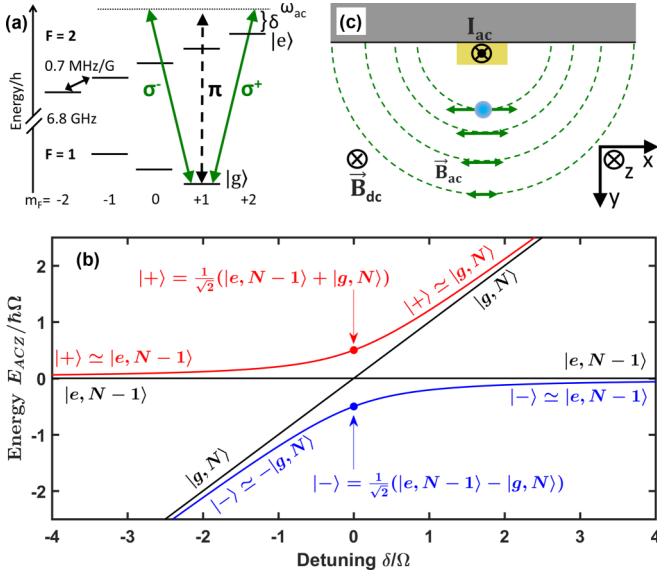
FIG. 1. Experimental scheme. (a) Hyperfine ground levels of ^{87}Rb ($5S_{1/2}$) and relevant transitions (green). (b) Plot of the eigenenergies E_{ACZ} (red and blue avoided crossing curves) for the $|\pm\rangle$ eigenstates versus μw detuning δ, along with the energies of the dressed-atom basis states (black). (c) Atom chip setup. An ODT confines atoms (blue dot) a distance $d \approx 100\ \mu$m below a z-axis wire (yellow), which supports a 6.8 GHz current I_{ac} that generates the μw magnetic near-field $\vec{B}_{ac}$.

As shown in Fig. 1(b), the two basis states (black lines) differ in energy by $\hbar\delta$, but are degenerate on resonance. The interaction between the μw field and the atom produces two energy eigenstates that are linear combinations of the basis states: a weak-field seeking $|+\rangle$ state and a strong-field seeking $|-\rangle$ state [15]. Figure 1(b) shows that once the interaction is included, the on-resonance degeneracy of the basis state energy levels becomes an avoided crossing for the $|\pm\rangle$ eigenstates (red and blue lines). The system can be made to travel along either eigenenergy curve by an adiabatic rapid passage (ARP) sweep of δ. For example, $|e, N-1\rangle$ can access the $|-\rangle$ ($|+\rangle$) eigenstate at any δ by sweeping from a large positive (negative) initial detuning.

A spatially varying $\vec{B}_{ac}(\vec{r})$ results in an ACZ energy [15] gradient and the following ACZ force for $|\pm\rangle$:

$$\vec{F}_{ac,|\pm\rangle} = \pm\frac{\hbar}{2}\frac{\Omega}{\sqrt{\delta^2 + \Omega^2}}[-\vec{\nabla}\Omega(\vec{r})], \qquad (1)$$

where $\Omega(\vec{r}) = \langle g| - \vec{\mu}\cdot\vec{B}_{ac}(\vec{r})|e\rangle/\hbar$ is the Rabi frequency and B_{ac} is the amplitude of the ac magnetic field. Neglecting the nuclear spin, the magnetic moment is $\vec{\mu} = (2\mu_B/\hbar)\vec{S}$, where μ_B is the Bohr magneton and $\vec{S}$ is the valence electron spin operator.

A sketch of the experimental setup and coordinate system are shown in Fig. 1(c). A thermal cloud of 10^5 ultracold ^{87}Rb atoms in $|e\rangle$ is transferred from an atom chip micromagnetic trap [21] into an optical dipole trap (ODT) located roughly 100 μm below the chip's surface. The ODT consists of two crossed 1064 nm laser beams: a 1.2 W beam directed along $\hat{z}$ with a $1/e^2$ waist radius of 60 μm and a 0.8 W beam along $\hat{x}$ (with a small $\hat{y}$ component) with a waist radius of 120 μm. The

resulting cigar-shaped ODT has trapping frequencies $\omega_{(x,y,z)} = 2\pi \times (186, 164, 28)$ Hz, a calculated depth of 23 μK, and atoms in $|e\rangle$ at 0.32 μK with calculated rms radius $\sigma_{x,y} \simeq 5\ \mu$m. A uniform magnetic field B_{dc} defines the quantization z axis for atomic spin states. Gravity is down along $\hat{y}$.

We generate the μw magnetic near-field B_{ac} by directing 6.8 GHz microwaves from a 3 W amplifier into a z-axis wire above the atoms [see Fig. 1(c)]. Due to significant losses in the amplifier-to-chip cabling, only a small fraction ($\sim$15%) of the μw power makes it to the chip. Furthermore, we do not impedance match the microwaves to the chip and so suffer additional loss due to reflection. Nevertheless, the generated μw current I_{ac} is sufficiently large to produce a significant B_{ac} and ACZ force. The chip wire into which we direct the μw power is roughly in the form of a "U": the central segment is along the z axis directly above the atoms, as shown in Fig. 1(c), with length 2 mm, width 50 μm, and thickness 3 μm. The resulting B_{ac} is expected to be primarily polarized along $\hat{x}$ at the atoms and drive $\sigma^{\pm}$ transitions ($\Delta m_F = \pm 1$). Stray polarization along $\hat{z}$ drives π transitions ($\Delta m_F = 0$), as shown in Fig. 1(a). The μw current distribution in neighboring wires (due to capacitive and inductive coupling) is not known, but its effect on the near-field B_{ac} at the atoms is included when one measures Ω and $\vec{\nabla}\Omega$.

III. ac ZEEMAN FORCE

We measure the ACZ force by turning off the ODT and applying a μw pulse of duration $t_{\mu w} = 0.5$ ms. The resulting ACZ impulse to the atoms is along $\hat{y}$ ($\pm 5°$). We measure the impulse velocity $\Delta v = \Delta y/\Delta t$ by absorption imaging of atoms in $|e\rangle$ for a time of flight $\Delta t = 12.25$ ms; Δy is the change in the atoms' y position due to the μw pulse [see Figs. 2(a) and 2(b)]. As a first approximation, we assume that the cloud size and $t_{\mu w}$ are sufficiently small that the ACZ force is constant in space and time over the duration of the pulse. The force is given by $F_{ac} = m\Delta v/t_{\mu w}$ with m as the mass of an atom.

We can apply the μw pulse with or without an ARP sweep. For the no-ARP case, the μw pulse is applied directly to atoms in $|e\rangle$ at a fixed δ, and the cloud splits in two [see Fig. 2(a), no ARP] according to the projection of $|e\rangle$ onto the $|+\rangle$ (push-down) and $|-\rangle$ (pull-up) states. If a brief ARP sweep (0.1 ms) is added to the start of the μw pulse, then the atoms are prepared in one of the $|\pm\rangle$ states, and the entire cloud experiences either a "push" or a "pull." The ARP sweeps start at a large initial detuning $\delta_0 = \pm 13$ MHz to populate the $|\mp\rangle$ state and end at the μw pulse detuning δ_{exp}. The ARP frequency ramp is sufficiently slow compared to the Rabi frequency ($|d\delta/dt| \ll |\Omega|$) that atoms initially in $|e\rangle$ travel adiabatically along the $|+\rangle$ ($|-\rangle$) eigenenergy curve in Fig. 1(b) for an upward (downward) sweep of the detuning. Since the ACZ force is "on" during a frequency ramp, the addition of an ARP sweep increases the impulse imparted to the atoms by 5% for $\delta_{exp} = 0$ to 20% at $\delta_{exp} = \pm 13$ MHz.

The Fig. 2(b) plot shows our ACZ force measurements as a function of δ for 3 W of μw power and $B_{dc} = 5.1$ G. The left axis shows the vertical displacement Δy produced by the ACZ impulse. In the no-ARP case, the ACZ force is proportional to Δy and is indicated on the right axis. This
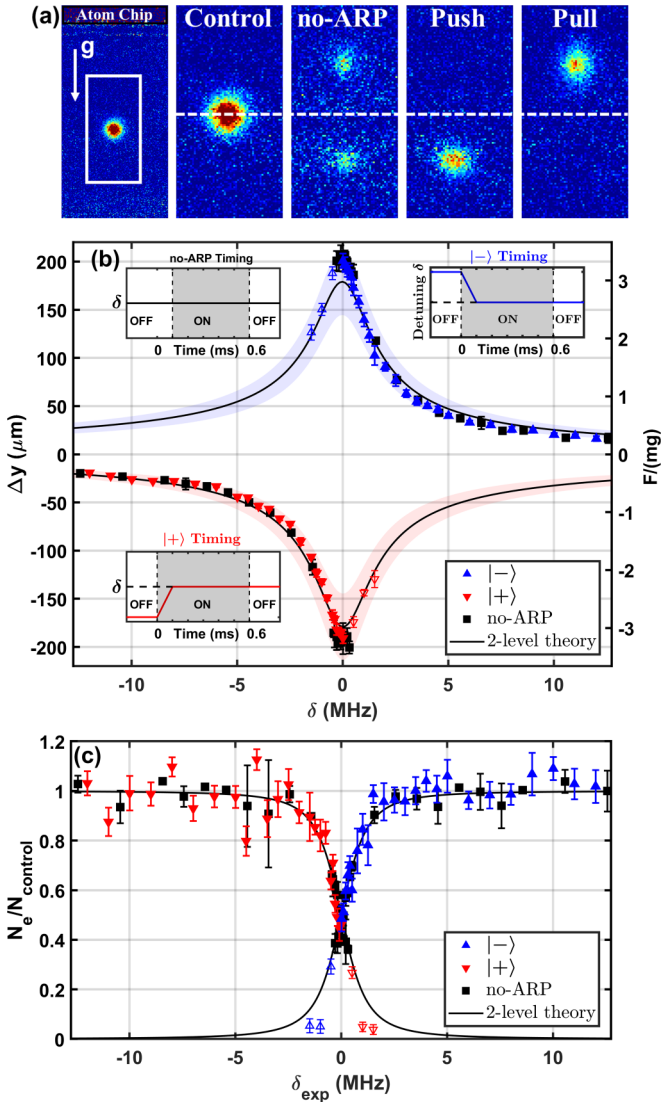
FIG. 2. ac Zeeman force measurement. (a) Sample of false color absorption images used in (b),(c). Atom chip: μw off and zoom-in box for other images. Control: μw off. no-ARP, Push, and Pull: resonant μw pulse ($\delta = 0$) with atoms in $|e\rangle$, $|+\rangle$, and $|-\rangle$, respectively. (b) Atom cloud displacement Δy vs μw detuning δ with an ARP sweep to constrain atoms to the $|\pm\rangle$ eigenstates (triangles) and with no sweep (no-ARP, squares). The right axis is the ACZ force for the no-ARP case and is approximately correct for $|\pm\rangle$ data. The black curves are not fits but predictions ($\pm 1\sigma$ shading) for Δy based on Eq. (1) and independently measured values for Ω and $d\Omega/dy$, including the impulse generated from the ARP sweep. *Insets:* detuning vs time during the μw pulse (ON) for the "no-ARP," $|+\rangle$, and $|-\rangle$ state preparation cases. (c) Atom number in $|e\rangle$ vs δ relative to control data without a μw pulse. The black curves are predictions [15] using the independently measured value for Ω and assume an instantaneous turn-off time. Data points are averages of five measurements; error bars give the standard deviation of the mean. The six open triangles in (b),(c) were analyzed differently due to low signal.

proportionality (and the right axis) is only approximately correct for ARP-based measurements because of the applied force during the ARP sweep. The two-level theory curves (see the Appendix) use Eq. (1) to plot the expected Δy including

the ARP sweep and employ no free parameters. The theory curve uses $\Omega = 2\pi \times 1.284(22)$ MHz and $d\Omega/dy = 2\pi \times 12.0(2.3)$ kHz/μm, which are inferred values for 3 W based on Rabi oscillations measurements with 30 mW of μw power. We note that if we assume a $1/d$ dependence for B_{ac}, then this value for Ω implies a μw current $I_{ac} = 37$ mA rms. We determine $d\Omega/dy$ from additional Rabi oscillation measurements 11 μm below the standard ODT position. The $\pm 19\%$ (1σ) uncertainty in the prediction is shown by the colored bands. The two-level theory agrees reasonably well with the data, though on resonance (off resonance) the force is a little larger (smaller) than expected. A two parameter fit removes the discrepancy between theory and data by reducing Ω and increasing $d\Omega/dy$ each by 20% from their measured values.

Figure 2(c) shows the fraction of the atoms in $|e\rangle$ vs δ for the Fig. 2(b) data. We integrate the absorption images used for the Fig. 2(b) data to obtain the atom number in $|e\rangle$ for both the ARP and no-ARP cases. Control images with no μw pulse and thus with all atoms in $|e\rangle$, taken immediately before and after the Fig. 2(b) data run, are used to determine the average total number of atoms $N_{control}$. The μw turn-off time is a little under 20 ns and negligibly affects the atomic populations. The two-level theory curves (see the Appendix) assume an instantaneous μw turn-off and show the expected fraction of atoms in $|e\rangle$: $|\langle e|\pm\rangle|^2$. The two-level theory matches the data, though ARP sweeps through resonance show some deviation. Taken together, Figs. 2(b) and 2(c) highlight that near resonance the ACZ force is strong but at the cost of mixing the $|g\rangle$ and $|e\rangle$ states. Off resonance, the ACZ force is reduced, but the $|g\rangle$ and $|e\rangle$ states experience much less mixing. In fact, the ACZ potential falls off as $\hbar|\Omega|^2/4\delta$, while the fractional population mixing falls off faster with detuning as $|\Omega/2\delta|^2$, similar to the ac Stark effect in optical dipole traps.

IV. TIME EVOLUTION

Next, we study the long-term time evolution of the $|\pm\rangle$ ACZ eigenstates with an eye towards future applications of ACZ potentials, such as trapping and spin-dependent positioning of atoms. Specifically, we determine the extent to which $|\pm\rangle$ atoms (in ODT) acquire a $|\mp\rangle$ component over time, whether from single-particle physics or collisions. However, due to rapid loss for atoms prepared in $|+\rangle$ (with $\delta \lesssim 0$), we focus primarily on the stability of atoms initially in $|-\rangle$ (with $\delta \gtrsim 0$), which evolve more slowly. We do not have an explanation for this difference in behavior between the two states, but it appears to be due to single particle physics, as we do not observe a change in the atom loss rate with collision rate.

We use a weak ACZ force produced by 20 mW of μw power to limit spin-dependent evaporation from the ODT: $F_{ac}(\delta = 0)$ and Ω in Fig. 2(b) are reduced by a factor of 13, resulting in a spin-dependent variation in trap depth of $\pm 9\%$ for the $|\mp\rangle$ states. Figure 3(a) shows the experimental timing sequence. We transfer atoms in $|e\rangle$ to $|-\rangle$ with a 20 ms ARP sweep (ARP1) and then keep the μw power and δ fixed for a variable hold time, during which atoms may evolve a $|+\rangle$ component. A reverse ARP sweep (ARP2) maps the $|-\rangle$ ($|+\rangle$) component onto $|e\rangle$ ($|g\rangle$). The 1.5-ms-long ARP3 sweep transfers atoms in $|g\rangle$ to the $|2,0\rangle$ state. The ODT is then turned off, followed by a brief dc Stern-Gerlach pulse, and a 0.1 ms laser "prepulse"
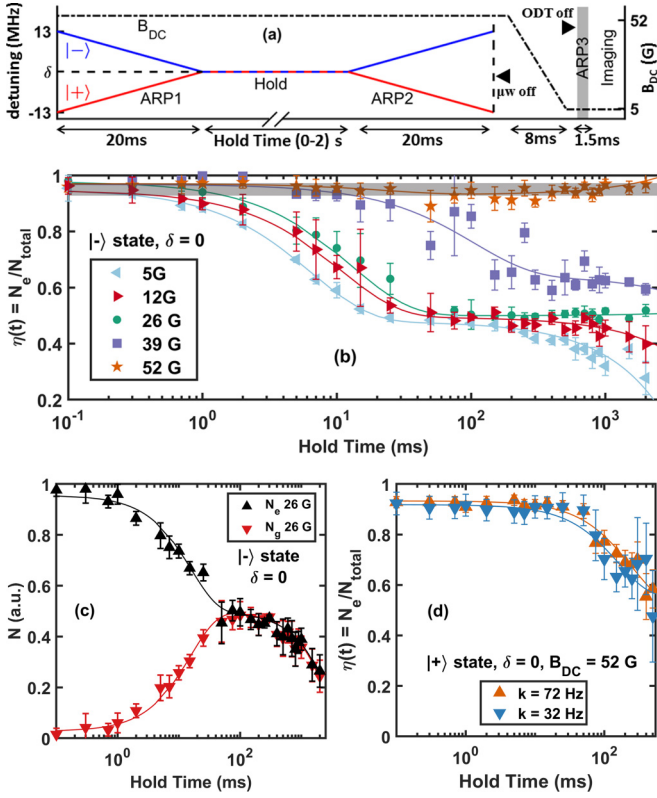
FIG. 3. Time evolution of the ACZ eigenstates. (a) Timing sequence showing the preparation of the $|\pm\rangle$ states (ARP1), variable hold time t, mapping back to the $|e\rangle$ and $|g\rangle$ states (ARP2), and the transfer of atoms in $|g\rangle$ to $|2,0\rangle$ for imaging (ARP3). The right y axis and dash-dot line shows an example of B_{dc} timing for $B_{dc} = 52$ G. (b) Plot of the fraction of atoms in $|-\rangle$, $\eta(t)$, versus t for different B_{dc} at $\delta = 0$. The gray band indicates the range of $\eta(t)$ scatter for no microwaves. The solid lines represent fits using the Eq. (2) model. (c) Atom numbers N_e and N_g in $|e\rangle$ and $|g\rangle$, respectively, versus t for $B_{dc} = 26$ G and $\delta = 0$. (d) Plot of $\eta(t)$ in the $|+\rangle$ case at two different collision rates k with $\delta = 0$ and $B_{dc} = 52$ G. The time axes are plotted on a log scale for (b)–(d) to highlight the difference between the exponential and linear decays.

to optically pump all of the atoms to $|2,2\rangle$ before the formal absorption imaging probe pulse. We measure the fraction of atoms in $|-\rangle$, $\eta = N_e/(N_g + N_e)$, by simultaneously imaging the $|e\rangle$ and $|g\rangle$ populations N_e and N_g.

Figure 3(b) shows the $\delta = 0$ time evolution of η at several B_{dc} for atoms initially in $|-\rangle$. We take an empirical approach and find that the data can be approximately described by an initial exponential-like fast decay (amplitude A and decay time τ) from $\eta \simeq 1$ to $\eta = \eta_f$, followed by a much slower decay, which is roughly linear out to 2 s (slope $-\beta$). During the initial fast decay, we observe transfer of atoms between the two eigenstates, but with little atom loss from the ODT. In contrast, the slower decay described by β is characterized by spin-dependent atom loss from the ODT. We model the data with the following function:

$$\eta(t) = \eta_f + A\,e^{-t/\tau} - \beta t. \quad (2)$$

This equation describes the observed behavior reasonably well, but with clear deviations in some cases. For instance,
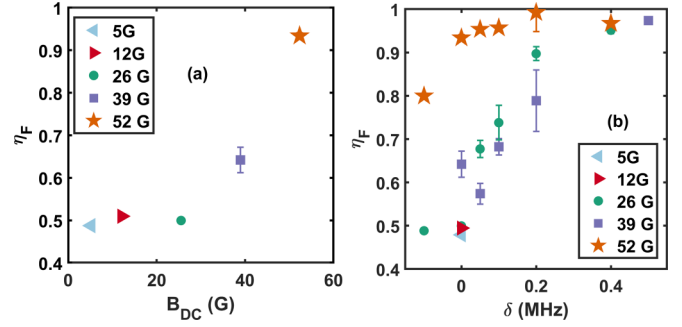

FIG. 4. Behavior of η_f with magnetic field and detuning extracted from fitting $\eta(t)$ data to Eq. (2). (a) Plot of η_f, the short-term decay floor for η, versus B_{dc} for $\delta = 0$. (b) Plot of η_f versus μw detuning δ for different B_{dc}.

the initial decay can feature momentary increases as seen in Fig. 3(b) at 39 G. The most reliable behavior is the settling of η to η_f after the initial decay, which we explore further. Figure 4(a) summarizes the behavior of η_f with magnetic field (at $\delta = 0$) and shows that atoms tend to stay in $|-\rangle$ for large B_{dc}, while fields below 26 G lead to equal populations in the two eigenstates. The detuning dependence of η_f also varies with B_{dc}: Fig. 4(b) shows that η_f decreases significantly for $\delta \lesssim 0.4$ MHz, but that for large B_{dc} the decrease is less pronounced and occurs for $\delta \lesssim 0$ MHz.

Finally, we find that $\eta(t)$ does not depend on density. At 52 G with $|-\rangle$ atoms at $t = 2$ s, we measure $\eta_f = 0.90(1)$ and $0.91(2)$ for densities of 9.6×10^{12} cm^{-3} and 7.5×10^{12} cm^{-3} (collision rate $k = 35$ and 22 Hz), respectively. Likewise, the evolution of η for atoms initially in $|+\rangle$ in Fig. 3(d) does not depend on collision rate. These null results imply that the observed evolution is due to single particle physics, rather than collisions. We obtain a shorter τ when the μw linewidth is increased at low B_{dc} with $\delta = 0$, indicating that detuning jitter (e.g., from ω_{ac} or B_{dc}) may contribute to the eigenstate evolution at short times. We do not have a model to explain the observed mixing of the eigenstates documented in Fig. 3 and Fig. 4. However, since the on-resonance splitting of the dressed-atom eigenstates is $\Omega = 2\pi \times 105$ kHz (at 20 mW of μw power), we speculate that detuning noise at this frequency or at odd subharmonics [22,23] could drive transitions between the eigenstates, thus accounting for the fast decay to η_f. An avenue for future study of the eigenstate mixing is to use a spatially flat μw field, so that Ω can be varied to determine its role, but without risk of spin-dependent evaporation from the ODT.

We have also made an initial study of the time evolution of atoms prepared in $|+\rangle$ and find that its short-term behavior features a sharp "knee" that initiates the decay, at approximately 55 ms in Fig. 3(d) plot of $\eta(t)$ for $|+\rangle$ at 52 G. Its long-term evolution shares the general features of the $|-\rangle$ case decay: η_f is larger for increasing magnetic field B_{dc}, as well as increasing detuning δ, and shows no density dependence. However, the $|+\rangle$ data is noisier due to qualitatively faster trap losses and heating, thus limiting the reliable extraction of fit parameters. Furthermore, the sharp knee (at which point the decay begins), is unexplained and is a subject for further investigation. This behavior suggests a possible technical issue, but we have been unable to determine its cause.
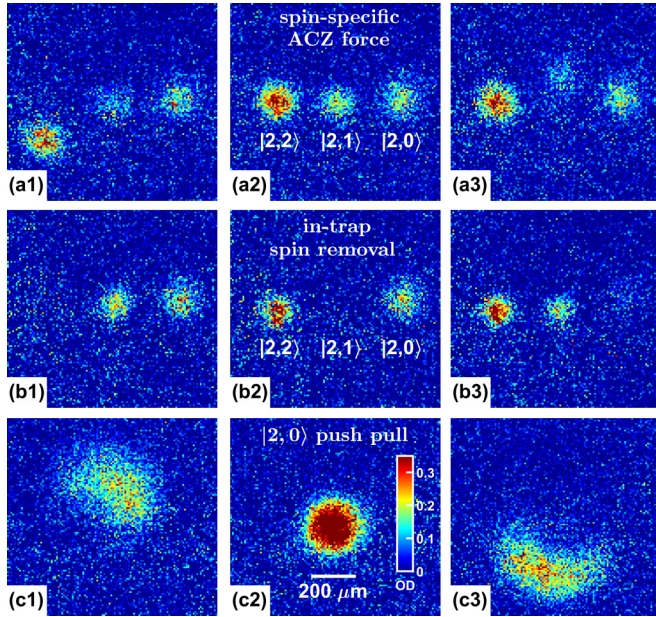
FIG. 5. Demonstrations of spin selectivity. (a) Spin-specific targeting of the ACZ force to an untrapped spin-mixture using the procedure and orientation of Fig. 2(b). A 0.5 ms ACZ impulse (a1) pushes down $|2,2\rangle$, (a2) is off, and (a3) pulls up $|2,1\rangle$. The spins are separated horizontally after the ACZ force is applied. (b) Targeted removal of spin states from a spin mixture in the ODT with $F_{ACZ} \simeq 3mg\,\hat{y}$ applied for 5 ms. (c) The ACZ force applied to atoms in $|2,0\rangle$: a 0.5 ms impulse (c1) pulls up, (c2) is off, and (c3) pushes down. All the false color images share the same length scale and optical depth color scale, given in (c2). In all frames, the ACZ force is applied with 3 W of μw power and $\delta = 0$. We use $B_{dc} = 52$ G along the z axis for frames (a1)–(a3) and (b1), and $B_{dc} = 46$ G along the x axis for frames (b2),(b3) and (c1)–(c3).

V. SPIN-SPECIFIC FORCE

A useful feature of the ACZ force is the ability to target a specific spin-state transition pair while leaving other states largely unaffected. In Fig. 5(a), we release atoms in a spin mixture of $|2,2\rangle$, $|2,1\rangle$, and $|2,0\rangle$ states from the ODT, briefly apply a resonant ACZ force to one of the states, and then use a magnetic gradient pulse to separate the states horizontally (Stern-Gerlach effect) before imaging. An ACZ push targeted to the $|2,2\rangle$ state using the $|e\rangle \leftrightarrow |g\rangle$ transition is shown in Fig. 5(a1). In Fig. 5(a3), we apply an ACZ pull to the $|2,1\rangle$ state using the $|2,1\rangle \leftrightarrow |1,0\rangle$ transition [24]. For reference, the case of no ACZ force is shown in Fig. 5(a2). Alternatively, if the ACZ force is applied while the spin mixture is in the ODT, then we can selectively eject atoms of a given spin by pushing them out of the trap. Figure 5(b) shows the selective removal of the $|2,2\rangle$, $|2,1\rangle$, and $|2,0\rangle$ states from the ODT before Stern-Gerlach imaging.

The ACZ force can also be applied to atoms in magnetically insensitive spin states, such as $|2,0\rangle$, which are of metrological interest. Figure 5(c) shows the application of an ACZ force to untrapped atoms in $|2,0\rangle$. In contrast with the rest of this work, this ACZ force uses the π transition $|2,0\rangle \leftrightarrow |1,0\rangle$ with B_{dc} oriented along the x axis. The matrix element for this transition is somewhat larger than for the $|e\rangle \leftrightarrow |g\rangle$ transition, which results in a 15% stronger ACZ force. The higher initial

temperature of the atoms and larger cloud size contribute to the curved distortion of the pushed and pulled clouds. This scheme was also used in Fig. 5(b2) and Fig. 5(b3) by employing the $|2,1\rangle \leftrightarrow |1,1\rangle$ and $|2,0\rangle \leftrightarrow |1,0\rangle$ transitions, respectively.

VI. CONCLUSION

In conclusion, we have measured the ACZ force produced by a μw near field from an atom chip and found agreement with two-level dressed-atom theory [15]. The force is resonant and bipolar and can be targeted to a specific spin state. At 100 μm with a 3 W amplifier, the $\sim$3 mg force is sufficient for practical manipulations of ultracold atoms. Larger forces should be possible with improved μw impedance matching to the atom chip, higher μw power, or a shorter chip-atom distance. Our initial study on the continuous application of a μw near field shows that the long-term eigenstate stability improves with larger dc magnetic field and μw detuning. We note that we have also pushed atoms in a micromagnetic chip trap with a far off-resonance ACZ force (see also [17]) with little loss. ACZ potentials are well suited for spin or species specific spatial manipulation applications. For example, an ACZ force could enable sympathetic cooling in an ODT by selectively evaporating one atomic spin state or species within a mixture [25]. Alternatively, an ACZ force could be used for spin-dependent beam splitting [see Fig. 2(a)] and interferometry [17]. Finally, a local minimum in a μw near field could provide spin or species-specific trapping [26,27].

APPENDIX

The black two-level theory curves in Fig. 2(b) give the variation in vertical position Δy of the atoms due to the applied ac Zeeman impulse. The curves include the contribution to the atom's impulse by the $t_{ARP} = 0.1$ ms ARP sweep and the $t_{\mu w} = 0.5$ ms fixed detuning portion of the μw pulse. The impulse from the ARP sweep is calculated by inserting a linear ramp $\delta(t) = \delta_0 + (\delta - \delta_0)t/t_{ARP}$ and then integrating Eq. (1) with respect to time from $t = 0$ to $t = t_{ARP}$. The impulse at fixed detuning is given by $F_{ac} t_{\mu w}$. The travel distance Δy (vertical) due to the impulse is obtained by multiplying the impulse by the time of flight Δt and dividing by the mass m of the atom:

$$\Delta y_{\pm} = \Delta y_{ARP} + \Delta y_{\mu w}$$

$$= \pm \frac{\hbar}{2} \Omega \frac{d\Omega}{dr} \frac{\Delta t}{m} \left\{ \frac{t_{ARP}}{\delta - \delta_0} \ln\left(\frac{\delta + \sqrt{\Omega^2 + \delta^2}}{\delta_0 + \sqrt{\Omega^2 + \delta_0^2}} \right) \right.$$

$$\left. + \frac{t_{\mu w}}{\sqrt{\Omega^2 + \delta^2}} \right\} \tag{A1}$$

The black two-level theory curves in Fig. 2(c) give the fraction of atoms in the $|e\rangle$ state for the ac Zeeman impulse measurements in Fig. 2(b). In the measurements with an ARP sweep, the atoms are placed in either the $|+\rangle$ or $|-\rangle$ eigenstate, and the probability to find an atom in $|e\rangle$ is given by [15]

$$P(e|+) = |\langle e|+\rangle|^2 = (\Omega' - \delta)^2/\xi^2, \qquad (A2)$$

$$P(e|-) = |\langle e|-\rangle|^2 = \Omega^2/\xi^2, \qquad (A3)$$

with $\Omega' = \sqrt{\delta^2 + \Omega^2}$ and $\xi = \sqrt{\Omega^2 + (\Omega' - \delta)^2}$. In the case of the "no-ARP" measurements, we measure the fraction of atoms in $|e\rangle$ that have been pushed down from the chip, and thus projected onto the $|+\rangle$ state with probability $P(+|e) = |\langle+|e\rangle|^2$ given by Eq. (A2). The fraction of atoms in $|e\rangle$ that have been pulled up towards the chip have been projected onto the $|-\rangle$ state with probability $P(-|e) = |\langle-|e\rangle|^2$ given by Eq. (A3).

[1] N. F. Ramsey, Phys. Rev. **78**, 695 (1950).

[2] R. Wynands and S. Weyers, Metrologia **42**, S64 (2005).

[3] S. Bize, P. Laurent, M. Abgrall, H. Marion, I. Maksimovic, L. Cacciapuoti, J. Grünert, C. Vian, F. Pereira dos Santos, P. Rosenbusch, P. Lemonde, G. Santarelli, P. Wolf, A. Clairon, A. Luiten, M. Tobar, and C. Salomon, J. Phys. B: At., Mol., Opt. Phys. **38**, S449 (2005).

[4] A. D. Ludlow, M. M. Boyd, J. Ye, E. Peik, and P. O. Schmidt, Rev. Mod. Phys. **87**, 637 (2015).

[5] W. Happer, Rev. Mod. Phys. **44**, 169 (1972).

[6] H. F. Hess, G. P. Kochanski, J. M. Doyle, N. Masuhara, D. Kleppner, and T. J. Greytak, Phys. Rev. Lett. **59**, 672 (1987).

[7] H. J. Metcalf and P. van der Straten, *Laser Cooling and Trapping* (Springer, New York, 1999).

[8] W. Ketterle, D. S. Durfee, and D. M. Stamper-Kurn, in *Proceedings of the International School of Physics Enrico Fermi* (IOS Press, Amsterdam, 1999), pp. 67–176.

[9] N. Lundblad, M. Schlosser, and J. V. Porto, Phys. Rev. A **81**, 031611 (2010).

[10] C. Y. Park, J. Y. Kim, J. M. Song, and D. Cho, Phys. Rev. A **65**, 033410 (2002).

[11] O. Mandel, M. Greiner, A. Widera, T. Rom, T. W. Hänsch, and I. Bloch, Phys. Rev. Lett. **91**, 010407 (2003).

[12] M. Bloom and K. Erdman, Can. J. Phys. **40**, 179 (1962).

[13] M. Bloom, E. Enga, and H. Lew, Can. J. Phys. **45**, 1481 (1967).

[14] S. R. Leslie, J. Guzman, M. Vengalattore, J. D. Sau, M. L. Cohen, and D. M. Stamper-Kurn, Phys. Rev. A **79**, 043631 (2009).

[15] C. C. Agosta, I. F. Silvera, H. T. C. Stoof, and B. J. Verhaar, Phys. Rev. Lett. **62**, 2361 (1989).

[16] R. J. C. Spreeuw, C. Gerz, L. S. Goldner, W. D. Phillips, S. L. Rolston, C. I. Westbrook, M. W. Reynolds, and I. F. Silvera, Phys. Rev. Lett. **72**, 3162 (1994).

[17] P. Böhi, M. F. Riedel, J. Hoffrogge, J. Reichel, T. W. Hänsch, and P. Treutlein, Nat. Phys. **5**, 592 (2009).

[18] C. Ospelkaus, U. Warring, Y. Colombe, K. R. Brown, J. M. Amini, D. Leibfried, and D. J. Wineland, Nature (London) **476**, 181 (2011).

[19] T. P. Harty, D. T. C. Allcock, C. J. Ballance, L. Guidoni, H. A. Janacek, N. M. Linke, D. N. Stacey, and D. M. Lucas, Phys. Rev. Lett. **113**, 220501 (2014).

[20] T. Schumm, S. Hofferberth, L. M. Andersson, S. Wildermuth, S. Groth, I. Bar-Joseph, J. Schmiedmayer, and P. Krüger, Nat. Phys. **1**, 57 (2005).

[21] M. K. Ivory, A. R. Ziltz, C. T. Fancher, A. J. Pyle, A. Sensharma, B. Chase, J. P. Field, A. Garcia, D. Jervis, and S. Aubin, Rev. Sci. Instrum. **85**, 043102 (2014).

[22] R. J. C. Spreeuw and J. Woerdman, Prog. Opt. **31**, 263 (1993).

[23] R. Graham and M. Höhnerbach, Phys. Lett. A **101**, 61 (1984).

[24] The $|2,0\rangle$ state is pulled slightly in Fig. 4(a3), due to the quasidegeneracy of the $|2,1\rangle \leftrightarrow |1,0\rangle$ transition and weaker $|2,0\rangle \leftrightarrow |1,1\rangle$ transition.

[25] M. Brown-Hayes, Q. Wei, C. Presilla, and R. Onofrio, Phys. Rev. A **78**, 013617 (2008).

[26] L. J. LeBlanc and J. H. Thywissen, Phys. Rev. A **75**, 053612 (2007).

[27] J. Catani, G. Barontini, G. Lamporesi, F. Rabatti, G. Thalhammer, F. Minardi, S. Stringari, and M. Inguscio, Phys. Rev. Lett. **103**, 140401 (2009).